

## A Dramatic Decrease in Carbon Star Formation in M31

M. L. BOYER,<sup>1</sup> B. F. WILLIAMS,<sup>2</sup> B. ARINGER,<sup>3,4</sup> Y. CHEN,<sup>3</sup> J. J. DALCANTON,<sup>5</sup> L. GIRARDI,<sup>4</sup> P. GUHATHAKURTA,<sup>6</sup>  
P. MARIGO,<sup>3</sup> K. A. G. OLSEN,<sup>7</sup> P. ROSENFELD,<sup>8</sup> AND D. R. WEISZ<sup>9</sup>

<sup>1</sup>*STScI, 3700 San Martin Drive, Baltimore, MD 21218 USA*

<sup>2</sup>*Department of Astronomy, Box 351580, University of Washington, Seattle, WA 98195, USA*

<sup>3</sup>*Department of Physics and Astronomy Galileo Galilei, University of Padova, Vicolo dell'Osservatorio 3, I-35122 Padova, Italy*

<sup>4</sup>*Osservatorio Astronomico di Padova – INAF, Vicolo dell'Osservatorio 5, I-35122 Padova, Italy*

<sup>5</sup>*Department of Astronomy, Box 351580, University of Washington, Seattle, WA 98195, USA*

<sup>6</sup>*University of California Observatories/Lick Observatory, University of California, 1156 High St., Santa Cruz, CA 95064*

<sup>7</sup>*National Optical Astronomy Observatory, 950 North Cherry Avenue, Tucson, AZ 85719, USA*

<sup>8</sup>*Eureka Scientific, Inc., 2452 Delmer Street, Oakland CA 94602, USA*

<sup>9</sup>*Department of Astronomy, University of California Berkeley, Berkeley, CA 94720, USA*

### ABSTRACT

We analyze resolved stellar near-infrared photometry of 21 HST fields in M31 to constrain the impact of metallicity on the formation of carbon stars. Observations of nearby galaxies show that the carbon stars are increasingly rare at higher metallicity. Models indicate that carbon star formation efficiency drops due to the decrease in dredge-up efficiency in metal-rich thermally-pulsing Asymptotic Giant Branch (TP-AGB) stars, coupled to a higher initial abundance of oxygen. However, while models predict a metallicity ceiling above which carbon stars cannot form, previous observations have not yet pinpointed this limit. Our new observations reliably separate carbon stars from M-type TP-AGB stars across 2.6–13.7 kpc of M31's metal-rich disk using HST WFC3/IR medium-band filters. We find that the ratio of C to M stars (C/M) decreases more rapidly than extrapolations of observations in more metal-poor galaxies, resulting in a C/M that is too low by more than a factor of 10 in the innermost fields and indicating a dramatic decline in C star formation efficiency at metallicities higher than  $[M/H] \approx -0.1$  dex. The metallicity ceiling remains undetected, but must occur at metallicities higher than what is measured in M31's inner disk ( $[M/H] \gtrsim +0.06$  dex).

*Keywords:* galaxies: individual (M31)—infrared: stars—stars: AGB and post-AGB—stars: carbon—stars: evolution

### 1. INTRODUCTION

Stars with initial masses of  $\approx 0.8\text{--}8 M_{\odot}$  will pass through the thermally-pulsing Asymptotic Giant Branch (TP-AGB) phase at the end of their evolution. The TP-AGB phase not only determines the subsequent evolution of the star (primarily due to strong mass loss), but also has a considerable impact on the evolution and appearance of the host galaxy. TP-AGB stars are a significant contributor to galaxy chemical enrichment of light elements and heavy s-processes elements (Karakas & Lattanzio 2014; Fishlock et al. 2014; Cristallo et al. 2015) and to a galaxy's dust budget (Matsuura et al. 2009; Boyer et al. 2012; Zhukovska & Henning 2013; Schneider et al. 2014; Srinivasan et al. 2016). TP-AGB stars are also among the brightest objects in galaxies,

especially in the near-infrared, and thus contribute up to 70% of a galaxy's total integrated light (Melbourne et al. 2012; Melbourne & Boyer 2013). The physics of TP-AGB stars therefore has major implications for galaxy properties derived from rest-frame near-infrared light (e.g., Conroy et al. 2009; Johnson et al. 2013; Baldwin et al. 2017).

Unfortunately, TP-AGB stars are simultaneously important and notoriously difficult to model, due to complex processes such as pulsation (both dynamic and thermal), mass loss, convection, and dredge up. Adding to the difficulty is a dearth of observational constraints for AGB models. The paucity of usable observations is rooted in 1) small populations and small number statistics due to their short lifetime and 2) the historic difficulty in obtaining infrared observations of individual stars in star-forming galaxies in and beyond the Local Group.

Recent work has provided new advances in describing the TP-AGB phase in metal-poor environments (Ven-

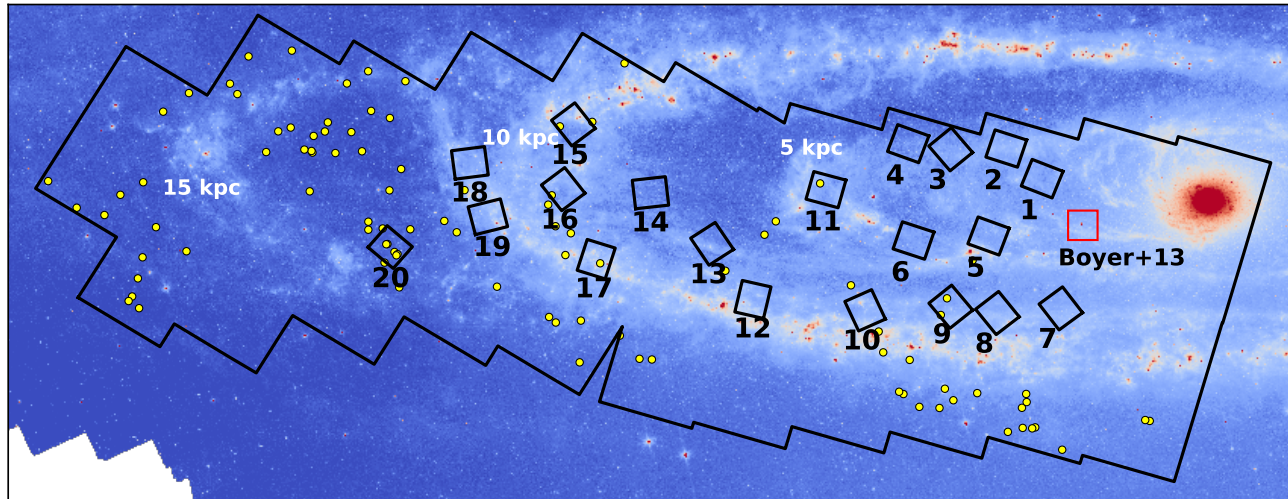


**Figure 1.** Spitzer 8- $\mu\text{m}$  image of M31 showing the PHAT footprint (outer black outline), the pilot field (red; B13), and the 20 fields observed here ( $136'' \times 123''$ ). Yellow dots are spectroscopically-confirmed carbon stars from SPLASH (Hamren et al. 2015). The approximate location of the 5, 10, and 15 kpc star-forming rings are marked for reference.

tura & Marigo 2010; Marigo et al. 2013; Rosenfield et al. 2014, 2016; Pastorelli et al. 2019; Nanni et al. 2016; Karakas et al. 2018), but metal-rich models remain poorly constrained. In the Milky Way, TP-AGB stars have intrinsically uncertain Gaia distances due to the motion of large convection cells (Chiavassa et al. 2011, 2018), making their infrared luminosities unreliable. This limitation makes it impossible to use Galactic TP-AGB stars to constrain high metallicity models. The next most nearby metal-rich environment is the Andromeda Galaxy (M31), which has recently been observed with high precision in the near-infrared by the Panchromatic Hubble Andromeda Treasury (PHAT) program (Dalcanton et al. 2012b). The PHAT program provides a large population of easily observable, high metallicity TP-AGB stars at a common distance.

In this work, we target several fields in the region of M31 observed by the PHAT program with observations designed specifically to identify the two main TP-AGB stellar types: carbon-rich (C type) and oxygen-rich (M type). Separating these two stellar types is key for calibrating the third dredge up process, which critically determines when a star becomes carbon rich and hence affects the onset of the final phases of enhanced mass loss. The formation of C stars is favored at low metallicities because (1) less oxygen is available to bind dredged-up carbon into the CO molecule, and (2) the depth of the third dredge up events increases at low metallicity (Karakas et al. 2002). This varying efficiency directly reflects in the ratio of C to M stars (C/M), which is observed to be anticorrelated with metallicity. At high metallicity, theoretical models indicate that the onset of the superwind phase terminates the TP-AGB phase before the star goes through enough dredge-up events to become C-rich (Weiss & Ferguson 2009; Marigo et al.

2013), resulting in a predicted metallicity ceiling for carbon star formation. The COLIBRI models (Marigo et al. 2013), for example, predict that this metallicity ceiling occurs somewhere between  $[M/H] = +0.1$  and  $+0.4$  (Boyer et al. 2013). However, the exact value of this upper limit in metallicity for the formation of C stars is highly sensitive to uncalibrated model details.

Here, we provide the first observations of TP-AGB stars in a metal-rich environment (M31) capable of providing comprehensive model calibrations of the third dredge up and the C star metallicity ceiling as a follow-up to the pilot program, described in Boyer et al. (2013). In this first paper, we describe the survey design (§2), the observations and stellar classification (§3), and describe the resulting C/M in the context of the other nearby galaxies (§4 and §5). We find that the carbon star formation efficiency decreases at a rate higher than expected based on observations in more metal-poor galaxies, but that the predicted metallicity ceiling for carbon star formation remains elusive. A forthcoming paper (Chen et al., in preparation) will explore the resulting constraints to the Padova TP-AGB models.

## 2. SURVEY DESIGN

We imaged 20 fields within the PHAT footprint with the WFC3/IR camera on the Hubble Space Telescope (HST) between July 2016 and Feb 2017 (GO-14072). Figure 1 displays a map of the fields, which we placed to sample a wide range in metallicity and age (§2), while also covering locations with spectroscopically-confirmed AGB stars (Hamren et al. 2015). We list the field information in Table 1, including an estimate of the deprojected radius which we compute assuming a position angle of  $38^\circ$ , inclination angle of  $74^\circ$  (Barmby et al. 2006), central position of R.A. =  $10^{\text{h}}06^{\text{m}}45.8^{\text{s}}$  and Dec. =  $41^{\circ}26'9.2''$ .

**Table 1.** Field Information & C and M Star Statistics

Field	PHAT Brick <sup>a</sup>	RA (J2000)	Dec (J2000)	PA (E of N)	[M/H] <sup>b</sup>	$R_{\text{deproj}}$ (kpc)	$N_{\text{C}}^{\text{c}}$	$N_{\text{M}}^{\text{c}}$	$N_{\text{spec}}^{\text{d}}$
Pilot (0)	3	00:43:21.66	+41:21:55.1	225°0	+0.058 ± 0.010	2.61	9	2511	0
1	5	00:43:18.49	+41:26:10.9	67°0	+0.053 ± 0.011	2.83	7	1971	0
2	5	00:43:18.33	+41:29:29.3	63°5	+0.027 ± 0.017	4.17	5	1254	0
3	7	00:43:31.67	+41:32:28.3	3°3	+0.013 ± 0.019	4.83	11	1224	0
4	7	00:43:40.58	+41:34:56.8	35°2	+0.000 ± 0.022	5.50	6	948	0
5	5	00:43:48.18	+41:26:22.4	65°1	+0.023 ± 0.017	4.34	4	1847	0
6	7	00:44:07.64	+41:30:09.3	65°0	−0.001 ± 0.022	5.56	10	1194	0
7	4	00:43:51.57	+41:19:12.6	32°4	−0.030 ± 0.028	7.00	22	1135	0
8	6	00:44:08.23	+41:22:22.1	66°8	−0.045 ± 0.031	7.77	20	961	0
9	6	00:44:17.65	+41:25:08.6	33°8	−0.048 ± 0.032	7.88	21	933	2
10	8	00:44:39.27	+41:29:32.6	70°0	−0.069 ± 0.036	8.96	31	731	0
11	9	00:44:13.99	+41:37:10.6	34°7	−0.012 ± 0.024	6.08	9	894	1
12	10	00:45:02.84	+41:36:00.3	20°0	−0.086 ± 0.039	9.82	23	686	0
13	11	00:44:57.09	+41:40:46.4	33°1	−0.063 ± 0.035	8.64	12	688	0
14	13	00:44:56.13	+41:46:17.2	272°0	−0.066 ± 0.035	8.82	16	578	0
15	15	00:44:55.97	+41:53:42.8	29°0	−0.101 ± 0.042	10.55	24	578	1
16	15	00:45:17.43	+41:51:13.7	342°5	−0.095 ± 0.041	10.25	35	627	1
17	14	00:45:29.18	+41:46:11.9	33°1	−0.105 ± 0.043	10.75	22	590	1
18	17	00:45:31.47	+41:57:16.3	338°0	−0.123 ± 0.047	11.67	19	448	0
19	16	00:45:42.86	+41:53:48.8	273°0	−0.123 ± 0.047	11.63	26	454	0
20	18	00:46:15.94	+41:57:27.1	280°0	−0.164 ± 0.055	13.68	14	189	5

NOTE— The pilot program ID is GO-12862, obtained in September 2012; the remaining 20 fields are from GO-14072, obtained between July 2016 and Feb 2017. The WFC3/IR field of view is 2'1 × 2'3. The DOI for this dataset is: 10.17909/t9-9xwn-et04.

<sup>a</sup> PHAT Brick (Dalcanton et al. 2012b)

<sup>b</sup> Metallicities are derived using the gradient measured by Gregersen et al. (2015). The uncertainties reflect the uncertainty in the gradient slope ( $\pm 0.004$  dex/kpc). The absolute metallicities are subject to systematics and assumptions and may vary by about 0.3 dex consistently across all fields.

<sup>c</sup>  $N_{\text{C}}$  and  $N_{\text{M}}$  are the number of C and M-type giants, respectively (§3.4).

<sup>d</sup> The number of carbon stars in the field identified via optical spectroscopy from Hamren et al. (2015).

(McConnachie et al. 2005), and distance of 776 kpc (Dalcanton et al. 2012b).

Data from the pilot program (Boyer et al. 2013) are also included here, and marked either as ‘pilot’ or ‘Field 0’ in tables and figures (outlined in red in Figure 1). Observations of the pilot field were taken in Sep 2012 (GO-12862). All analysis here includes a re-reduction of the pilot field, described in Section 3.

### 2.1. Metallicity

To study how metallicity affects C/M across M31’s disk, we adopt metallicities from Gregersen et al. (2015).

That work estimated [M/H] by interpolating isochrones over 7 million red giant branch (RGB) stars using the Padova PARSEC1.2s models (Bressan et al. 2012; Chen et al. 2014; Bressan et al. 2014) and spatially binning the results. They find an absolute offset compared to the BaSTI models (Pietrinferni et al. 2007), with the BaSTI models typically resulting in a metallicity higher by 0.3 dex over the full metallicity range.

Gregersen et al. (2015) investigated the age-metallicity degeneracy by testing different fiducial ages with and without age gradients in the disk. They find that the slope of the metallicity gradient is not affected by an

absolute offset in stellar age, but it shifts slightly (by  $\approx -0.003$  dex/kpc) if they assume a typical stellar age gradient ( $<|0.1|$  Gyr/kpc). The absolute metallicity is anticorrelated with RGB age, decreasing by  $\approx 0.2$  dex with a fiducial age of 12 Gyr. This, along with the offset found using the BaSTI models, suggests that while the relative metallicities between fields are reliable, the absolute values may vary by up to  $\pm 0.3$  dex.

While the absolute metallicity is somewhat uncertain, the spatial gradient in metallicity appears to be more robust. Overall, the [Gregersen et al. \(2015\)](#) analysis found a metallicity gradient of  $-0.020 \pm 0.004$  dex/kpc from  $\sim 4$ –20 kpc, assuming a mean RGB age of 4 Gyr. The [Gregersen et al. \(2015\)](#) slope is consistent with the slopes measured using H II regions over the same region of the disk ([Zurita & Bresolin 2012](#); [Sanders et al. 2012](#)), suggesting that the gradient is relatively stable over a long timescale. [Sanders et al. \(2012\)](#) find no abundance gradient from measurements of planetary nebulae (PNe), a population with a similar age to TP-AGB stars. However, they note that selection effects exclude higher metallicity PNe from their sample and conclude that the inclusion of metal-rich PNe would likely result in a metallicity gradient.

We extrapolate the metallicity gradient to the innermost fields that were not analyzed in [Gregersen et al. \(2015\)](#) due to crowding and incompleteness ( $\lesssim 3$  kpc). In these inner regions, [Saglia et al. \(2018\)](#) estimated the metallicities based on spatial maps of absorption line features fit with simple stellar population (SSP) models. Their spatial coverage reaches the position of our pilot program, for which they find  $[M/H] = -0.05$  to  $+0.05$ , consistent with the extrapolated value from the [Gregersen et al. \(2015\)](#) gradient. We list the adopted metallicities in Table 1.

## 2.2. Age

TP-AGB stars have initial masses of  $\approx 0.8$ – $8 M_{\odot}$ . All TP-AGB stars are initially M-type, while a subset eventually become carbon stars once enough carbon has dredged up to the surface. At M31’s metallicity, carbon TP-AGB stars are predicted to form only between ages of approximately 200 Myr and 4 Gyr ( $\approx 1.5$ – $4.5 M_{\odot}$ ; [Karakas & Lugaro 2016](#)), while the rest of the TP-AGB stars remain M-type. Therefore, we can only expect the C/M ratio to be a useful diagnostic if the stellar population spans the appropriate age range.

[Lewis et al. \(2015\)](#) and [Williams et al. \(2017\)](#) estimated the spatially-resolved star-formation history (SFH) across the disk by fitting stellar evolution models to PHAT color-magnitude diagrams (CMDs). They find that there are global star formation events from  $\approx 1.5$ –4 Gyr and at ages  $\gtrsim 8$  Gyr. The star-forming rings (Fig. 1) also contain a young component  $\lesssim 900$  Myr old. All of our fields contain a population from the global  $\approx 1.5$ –4 Gyr event ([Williams et al. 2017](#)), which produced carbon stars with initial masses around 1.5–

2.1  $M_{\odot}$ . We expect the bulk of the carbon stars in M31 to have formed during this event.

The ancient stellar population in M31, which is smoothly distributed from the bulge to the outer disk will contribute very few carbon stars. Since the bulge is dominated by this ancient population, we placed our innermost fields at a distance that minimizes the contribution of the bulge while also reaching the highest possible metallicity. Bulge stars are also enriched in He (e.g. [Nataf et al. 2011](#); [Rosenfield et al. 2012](#)), possibly due to pollution from an earlier population. He enrichment decreases the likelihood of carbon star formation even further by decreasing the stellar lifetime, resulting in fewer thermal pulses and less carbon dredge up ([Karakas 2014](#)). The PHAT optical CMDs (see §3.2) indicate that all of our fields, including those nearest the bulge, contain a strong contribution from a young population (also, [Lewis et al. 2015](#)). This suggests that the inner disk is a strong component in all of our inner fields, and thus carbon stars are expected to be present. In addition, we noted in [Boyer et al. \(2013\)](#) that the bulge is expected to contribute  $<30\%$  of the integrated *I*-band light in our pilot field ([Dorman et al. 2012](#)). Since the *I*-band is the least susceptible to stochastics from bright objects ([Melbourne & Boyer 2013](#)), the young inner disk is therefore the dominant population even in our most central fields.

## 2.3. Known AGB Stars

The Spectroscopic and Photometric Landscape of Andromeda’s Stellar Halo (SPLASH; [Dorman et al. 2012](#)) program obtained thousands of optical spectra ( $\lambda \sim 5000$ – $9000$  Å) in the disk using the DEIMOS spectrograph on the Keck II telescope. They found a total of 103 carbon stars and 736–1605 M stars, depending on how they are classified, based on the presence of CN and TiO absorption features ([Hamren et al. 2015](#)). Our fields contain 11 spectroscopically-confirmed carbon stars from the SPLASH survey, which provide a useful test of our photometric classification. These stars are marked in Figures 1 and 4 and noted in Table 1.

## 3. DATA & ANALYSIS

### 3.1. Observations

Each field in Table 1 was imaged with the F127M, F139M, and F153M filters on WFC3/IR. These filters are narrow enough ( $\Delta\lambda = 64$ – $69$  nm) to sample molecular features in TP-AGB stars and enable classification into C- and M-type giants ([Boyer et al. 2013, 2017](#)).

The WFC3/IR detector reads out continuously and non-destructively (multiaccum mode<sup>1</sup>). Here, we use the SPARS50 readout pattern, which samples the exposure ramp linearly with 50s intervals. Each field is

<sup>1</sup> WFC3 handbook: [http://www.stsci.edu/hst/wfc3/documents/handbooks/currentIHB/wfc3\\_cover.html](http://www.stsci.edu/hst/wfc3/documents/handbooks/currentIHB/wfc3_cover.html)

dithered to improve pixel sampling and mitigate effects from artifacts and/or cosmic rays. The exposures follow either a 2-pt or 4-pt WFC3-IR-DITHER-BOX-MIN pattern, which provides optimal PSF sampling. The total combined exposure time is 861.7s for F127M, and 855.9 s each for F139M and F153M.

### 3.2. Photometry & Crowding

We used the PHAT photometry pipeline, described in Williams et al. (2014). Briefly, we apply the point spread function (PSF) fitting package DOLPHOT (Dolphin 2000) to each of the 21 near-IR fields. First, each CCD readout of each exposure in all of the overlapping PHAT ACS/WFC and WFC3/IR data were run through the DOLPHOT PSF-fitting photometry routine along with each CCD readout of the new data. These single exposure catalogs were then put through an alignment routine to find a common astrometric solution for all of the exposures. This solution was applied to all of the headers in the original flat-fielded and CTE-corrected frames (f1c files for WFC exposures and f1t files for IR exposures). The exposures with updated astrometry were then run through the PyRAF routine `astrodrizzle` to generate deep stacked images and updated pixel masks. The pixel masks and area corrections were then applied to each CCD readout. Finally, these individual CCD readouts were simultaneously measured using the DOLPHOT PSF fitting routine, which finds stars using the full stack of all overlapping pixels in memory and forcing fits of the PSF at that sky location in every CCD read. All of these measurements were then combined in each band to optimize photometric depth.

The resulting photometry catalogs contain the measured brightness of each detected star along with several quality metrics of the measurement. These quality metrics were then used to clean the catalog of unreliable measurements using the `gst` criteria described in Williams et al. (2014). However, we found that the F127M filter contained some spurious detections with large `chi` values in the DOLPHOT output. Thus, we applied an additional criterion of `chi` < 4 for the F127M band.

Foreground extinction is low towards M31, especially in the near-IR. Nevertheless, all photometry presented in this paper is corrected for a mean foreground extinction using  $A_V = 0.1922$ , derived from the Schlegel et al. (1998) map and assuming  $R_V = 3.1$ . We adopt  $A_\lambda$  values listed in Table 2, computed as in Girardi et al. (2008) using the Cardelli et al. (1989) extinction curve with  $R_V = 3.1$ . We also verify that these coefficients change little (less than 2%) for stars covering a 2500 K range in  $T_{\text{eff}}$ .

Example optical and IR medium-band CMDs are shown in Fig. 2, including the innermost field, outermost field, and one intermediate field. The optical CMDs illustrate the relative ages of the fields, with  $\log(t_{\text{age}}/\text{yr})$

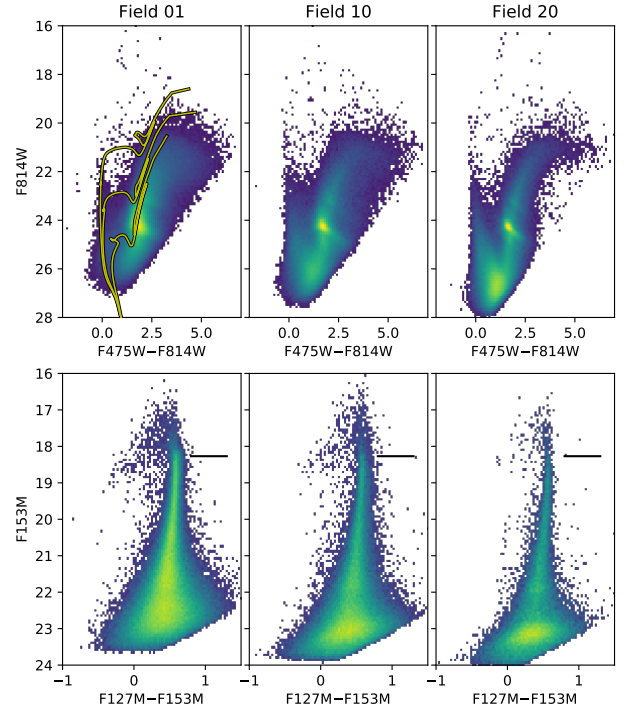


**Figure 2.** Sample optical and IR medium-band color-magnitude diagrams for the innermost field, outermost field, and one intermediate field. The optical CMDs (upper panels) illustrate both the variation in age and differential extinction. Parsec v1.2S isochrones (Bressan et al. 2012) with  $\log(t_{\text{age}}/\text{yr}) = 8, 8.5, \text{ and } 9$  and  $[M/H] = 0.119$  are included in the left panel (yellow lines). Differential extinction extends the RGB width towards the lower right. The IR CMDs (lower panels) illustrate a weaker impact from differential extinction. TP-AGB stars are mostly located above the tip of the RGB (TRGB), marked by a horizontal black line (§3.3), and extend towards fainter magnitudes at blue colors.

**Table 2.** Adopted  $A_\lambda$

Filter	$A_\lambda/A_V$ (mag)
F475W	1.185
F814W	0.610
F127M	0.274
F139M	0.240
F153M	0.204
F110W	0.337
F160W	0.204

= 8, 8.5, and 9 Parsec v1.2S isochrones included in the left panel (Bressan et al. 2012). The optical CMDs also illustrate the differential extinction, with the RGB width increasing towards the lower right, most visible in the red clump at  $F814W \approx 24$  mag; the extinction is lowest in the outer fields (e.g., Field 20 in the right panels). The medium-band CMDs are similar in all fields, with a smaller impact from differential extinction. TP-AGB stars occupy magnitudes brighter than  $F153M \approx 18$  mag and extend to fainter magnitudes at blue colors (§3.3 & 3.4).

Our most crowded field is the pilot field at 2.6 kpc, where the stellar density for stars with  $18.5 < F160W < 19.5$  mag ranges from 1.8–3 per arcsec<sup>2</sup>. In this regime, crowding dominates over other photometric uncertainties. Williams et al. (2014) showed that, for this stellar density in the PHAT data, the photometry begins to be biased slightly towards brighter magnitudes near 19–20 mag in F160W and the RMS uncertainty is near 0.2 mag, with slightly smaller values in F110W. We expect crowding to affect the photometry at similar limits in our most crowded fields, with a much weaker effect in regions farther out in the disk. Figure 3 shows the median and 1- $\sigma$  luminosity functions for F153M, the filter with the lowest resolution and strongest crowding. The crowding level is similar in most of our fields, with photometric completeness beginning to decrease around  $F153M = 22$ –23 mag, several magnitudes below the tip of the red giant branch (TRGB; §3.3). Only 3 fields (the pilot, 01, and 05) are more crowded than the 1- $\sigma$  luminosity function (red lines in Fig. 3), but even these are complete to  $\gtrsim 3$  mag fainter than the TRGB. Based on Williams et al. (2014), we expect the RMS error to be 0.1 mag or less in all but the inner  $\sim 3$  fields (in crowding order: the pilot field, field 1, and field 5). Since our C and M star selection criteria (§3.4) are restricted to stars brighter than the TRGB and well above the completeness limit, the uncertainties on the number of AGB stars are dominated by Poisson statistics rather than crowding or sensitivity limits.

### 3.3. TRGB

We must first select the TP-AGB stars before we can identify C- and M-giant stars. We do this by selecting stars that are brighter than the TRGB in at least one of the near-IR filters.

The RGB in our data is well-populated and unaffected by incomplete photometry to approximately 3 mag below the TRGB. We therefore follow the procedure described in Méndez et al. (2002) to measure the TRGB in each filter. We begin by constructing a luminosity function using a Bayesian optimization method to select the bin size.<sup>2</sup> To minimize the contributions from

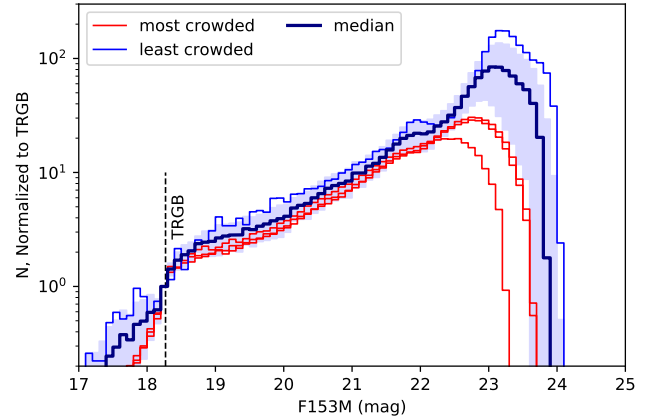


**Figure 3.** Median F153M luminosity function and 1- $\sigma$  range (shaded region), normalized to the TRGB. Only 3 fields (the pilot, and fields 01 and 05; in red) have luminosity functions that fall below the shaded region, indicating a higher level of incompleteness at faint magnitudes due to crowding. The thin blue line shows field 20, which is at the largest galactic radius and should therefore have the least amount of crowding among our fields.

foreground and main sequence stars to the luminosity function, we only include stars with  $F127M - F153M > 0.1$  mag. Next, we pass the Gaussian-smoothed luminosity function through a Sobel edge-detection filter to detect the TRGB, i.e., where the number of sources drops. We perform 500 Monte Carlo resampling trials to test the effect of random photometric errors and random variations in the bin sampling of the luminosity function. The resulting TRGBs, measured using all 21 fields simultaneously to avoid stochastics, are listed in Table 3.

The near-IR TRGB is known to vary with age and metallicity (e.g., Dalcanton et al. 2012a; McQuinn et al. 2017, 2019), and thus may not be constant across M31’s disk. In Table 3, we include the difference in the TRGB ( $\Delta$ TRGB) measured from the two innermost fields ( $\sim 2.7$  kpc,  $[M/H] \sim +0.05$ ) and two outer fields ( $\sim 11.6$  kpc,  $[M/H] \sim -0.12$ ). Given the relatively small range in metallicity, the TRGB difference between these two extremes is likewise small in all filters, less than 0.05 mag and typically on the order of the 1- $\sigma$  uncertainties. By using the TRGB in all five filters to select the initial sample of stars, we avoid any biases caused by differences in environment.

Most TP-AGB stars are brighter than the TRGB, though some can be fainter for the following reasons: (1) they are at the luminosity dip that characterizes the initial fraction of a thermal pulse cycle (Boothroyd & Sackmann 1988); (2) they have enough circumstellar dust to cause self-extinction; and/or (3) they have strong molecular absorption, with the particular molecule dependent on the filter. In our case, water absorption in M-giant

<sup>2</sup> [http://docs.astropy.org/en/stable/api/astropy.stats.knuth\\_bin\\_width.html](http://docs.astropy.org/en/stable/api/astropy.stats.knuth_bin_width.html)

**Table 3.** TRGB

Filter	$\lambda_{\text{pivot}}$ $\mu\text{m}$	TRGB (mag)	$1\sigma$ (mag)	$\Delta\text{TRGB}$ (mag)
F127M	1.27	18.80	0.04	0.05
F139M	1.38	18.66	0.03	0.03
F153M	1.53	18.27	0.01	0.05
F110W	1.15	19.28	0.02	0.01
F160W	1.54	18.28	0.02	0.01

NOTE— The TRGB is measured using all 21 fields simultaneously. The  $\Delta\text{TRGB}$  measurement is the absolute difference in the TRGB measured in two outer fields combined (Fields 18 & 19) and the two innermost fields combined (Fields 0 & 1); see text. Pivot wavelength is the effective filter wavelength, as quoted in the WFC3/IR handbook.

stars is the dominant effect causing TP-AGB stars to be fainter than the TRGB, since the broad water feature at  $1.4\ \mu\text{m}$  is covered to some degree by F139M, F153M, F110W, and F160W (see Fig. 1 in Boyer et al. 2013). F127M has the least overlap with this water feature and inspection of our data confirms that it has the fewest TP-AGB stars below its TRGB.

### 3.4. C and M Star Classification

To identify C- and M-type giants, we start by isolating the bulk of the TP-AGB stars by selecting stars that are brighter than the TRGB in at least one of the filters listed in Table 3. Next, we use the color-color diagram (CCD) in Figure 4 to divide the TP-AGB stars into C-type and M-type. This technique is described in detail in Boyer et al. (2013, 2017); it takes advantage of water absorption in M-giant stars and CN+C<sub>2</sub> absorption in carbon stars to create a remarkably clean separation of these stellar types in the medium-band filters. We largely use the color cuts from Boyer et al. (2017), illustrated in Figure 4, which isolate all M stars later than type M0. Main sequence, foreground, and K-type stars in our sample are removed by excluding objects on the lower-left region of the CCD. M31’s high metallicity leads its stars to have lower stellar temperatures, favoring the formation of cooler M-type stars over K-type stars on the AGB. As a result, many of the M31 CCDs show a clear gap between M-type and K-type stars near  $F139M - F153M = 0.3$  mag that was not seen in the metal-poor galaxies from Boyer et al. (2017) (e.g., Fields 0, 1, 2, 4, 6, 8, 14, & 20 in Figs. 12 and 13). We use this gap to slightly adjust the M star box down from the  $F139M - F153M = 0.35$  mag adopted by Boyer et al. (2017) to  $F139M - F153M = 0.3$  mag. Ta-

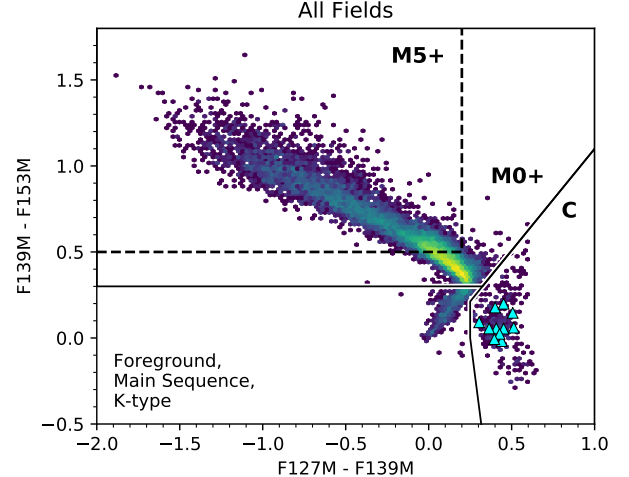


**Figure 4.** Medium-band color-color diagram showing the separation of C and M giant stars (solid line). We include only the 21,460 stars that are brighter than the TRGB in at least one of the filters listed in Table 3. Objects in the lower left box include contaminating objects (foreground, main sequence stars, and K-type AGB stars). Water absorption in M stars increases along the sequence towards the upper left, with late-type M giants showing the strongest water absorption (stars of type later than M5 are marked with a dashed line). Atmospheric C/O in C stars approximately increases towards the lower right. Circumstellar dust moves stars up and to the right while maintaining the separation between C and M stars (Boyer et al. 2017). Known C stars from the SPLASH program are marked by cyan triangles (Hamren et al. 2015).

ble 1 shows the resulting C and M star counts for each field.

The TRGB cuts used to select the initial subset of stars in Figure 4 may be missing a small fraction of TP-AGB stars. For example, the dustiest objects are faint or even undetected at  $1.5\ \mu\text{m}$  from self extinction. However, these objects are  $\lesssim 5\%$  of the total TP-AGB population and thus have only a small effect on C/M (Blum et al. 2006; Boyer et al. 2011, 2017). The fraction of very dusty stars does not appear to change much with metallicity, with both the LMC and SMC showing similar fractions, and thus M31 is not expected to be strongly affected. In addition, models suggest that dust production by C stars may be independent of metallicity (e.g., Nanni et al. 2013), also removing concerns that M31’s stars would be preferably dust enshrouded. Ideally, Mid-IR data would produce a complete TP-AGB census that includes all dust-producing stars, but in practice most estimates of C/M throughout the Local Group (e.g., Brewer et al. 1995; Battinelli & Demers 2005; Boyer et al. 2017; Cioni 2009, and references therein) use optical and/or near-IR data, and therefore also exclude the

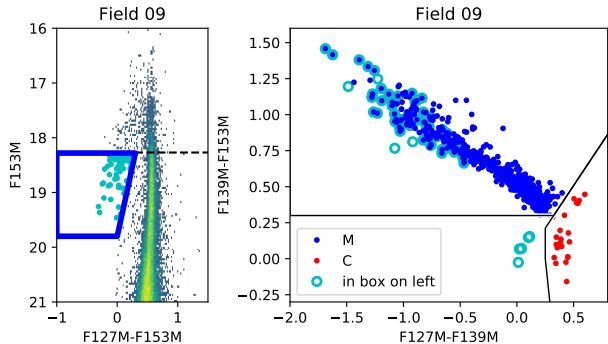


**Figure 5.** *Left:* We recover objects that are fainter than all five TRGBs due to deep water absorption by checking objects in the blue box, shown here for Field 09. The dashed line is the F153M TRGB. *Right:* Objects in the blue box on the left are plotted as open cyan circles, along with other C and M type stars. A handful of M stars in each field were recovered this way.

most extreme dusty objects that could be missing from this study of M31.

In addition to the dustiest objects, the starting TRGB criterion also misses a small number of sub-TRGB M giant stars with strong water absorption (§3.3). To recover these stars, we investigate sources in the blue box in Fig. 5. The lower and right-hand edges of the box are set to minimize the contamination from main sequence, foreground, and K-type stars; remaining interlopers are eliminated when plotted on the medium-band CCD. In total we recover 96 sub-TRGB M stars, which is  $\lesssim 1\%$  of the M giant population.

### 3.4.1. M Star Definition

Different M star definitions can make it challenging to compare the results from other C/M studies. In the metal-rich regime, different definitions can change the measured C/M by factors of  $\sim 1.5$ –4. Hamren et al. (2015) provide a comparison of the M-giant star definitions in M31 from Boyer et al. (2013), Brewer et al. (1995), and Battinelli & Demers (2005). The B95 and BD05 studies use a bolometric magnitude derived from  $V$ ,  $R$ , and  $I$  photometry to select the M-giant stars, as opposed to the near-IR TRGB method used here. The result is a dramatically different sample of M stars and a wide range in C/M. The definitions in B95 and BD05 are defined as:

$$\left. \begin{aligned} V - I > 1.8, \\ I > 18.5, \\ M_{\text{bol}} < -3.5, \text{ where} \\ M_{\text{bol}} = I + 0.3 + 0.34(V - I) \\ \quad - 0.14(V - I)^2 - (m - M)_0, \end{aligned} \right\} \text{B95} \quad (1)$$

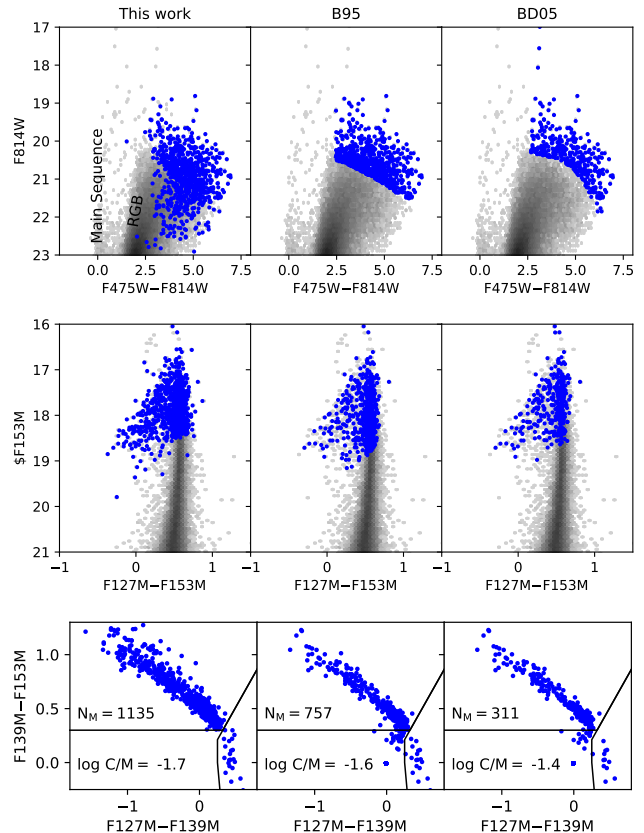


**Figure 6.** *Top:* Optical CMDs of Field 07, showing the M-giant population that results from the near-IR TRGB selection used here (left) and the  $M_{\text{bol}}$  selection used by B95 and BD05 (middle, right). *Middle:* Same, but for the near-IR CMDs. *Bottom:* The associated medium-band HST CCD showing the total number of M-giant stars ( $N_M$ ) for each strategy. All blue points in each CCD would be included in a C/M ratio, with B95 and BD05 including contaminating sources in the lower left box among their M star numbers. By restricting to  $M_{\text{bol}}$  derived from optical filters, late-type M stars with strong optical TiO absorption (and thus strong near-IR  $\text{H}_2\text{O}$  absorption) are excluded. This exclusion has an effect on C/M that is worse for higher metallicity fields that have a higher fraction of late-type M giants.

$$\left. \begin{aligned} R - I > 0.9, \\ M_{\text{bol}} < -3.5, \text{ where} \\ M_{\text{bol}} = I + 1.7 - 2.3(R - I) + \\ \quad 1.7(R - I)^2 - 0.4(R - I)^3 - \\ \quad (m - M)_0. \end{aligned} \right\} \text{BD05} \quad (2)$$

The resulting M star populations are illustrated for Field 7 in Fig. 6, using transformations from F814W and F475W HST magnitudes to  $V$ -,  $R$ -, and  $I$ -band magnitudes (Fluks et al. 1994; Sirianni et al. 2005; Hamren et al. 2015). By restricting the bolometric magnitude



of the sample (causing the sharp cut in blue points in the top middle/right panels of Fig. 6), a large number of late-type M stars with strong TiO absorption at 0.4–1  $\mu\text{m}$  are excluded from the cuts, resulting in a  $\sim 30$ –60% reduction in the total number of M stars compared to this work. By using the near-IR TRGB, especially in filters that are less susceptible to H<sub>2</sub>O absorption, our selection recovers these late-type M stars. The B95 and BD05 techniques also result in higher contamination from K-type stars, as indicated by the higher number of sources in the lower-left boxes of the CCDs in Figure 6.

Unlike in M31, late M-giant stars are rare in metal-poor environments ( $[M/H] < -1$ ; Boyer et al. 2017). As a result, all three M star definitions give similar C/M values in metal-poor galaxies, allowing for direct comparisons among multiple studies (§5.1).

#### 4. RESULTS

Here we present our results, first the discovery of a potential new metallicity diagnostic (C/O), then C/M across M31, which we expand on in Section 5.

##### 4.1. C/O and Metallicity

The ratio of atmospheric carbon to oxygen (C/O) increases with each dredge up event; if  $C/O > 1$ , a star is considered a carbon star. While a population at a given metallicity can span a wide range in C/O, a metal-rich population should show a lower C/O on average due to less efficient dredge up and a higher oxygen abundance.

Our medium-band filter set samples the strength of carbon features, and thus we can potentially use the medium-band colors as an approximate proxy for C/O in carbon stars. Carbon star atmosphere models from Aringer et al. (2009, 2016) predict that C/O increases roughly for C stars from the upper left to the lower right in the C star box of the medium-band CCD in Figure 4. We test this in figure 7, which shows the median F127M–F139M color of C stars plotted against metallicity. While the numbers are low in the most metal-rich regions, there is a clear trend for lower metallicity regions to have redder median colors. This suggests that the median F127M–F139M color of a C star population could be an efficient diagnostic for identifying metal-rich populations and for tracking metallicity gradients across galaxies. The best fit to the trend in Figure 7 is:

$$(F127M - F139M)_{\text{med}} = 0.39 - (0.52 \times [M/H]). \quad (3)$$

We note that, while both the C/O proxy and the metallicity in Figure 7 are derived from stellar colors, these measurements are independent. Metallicity is measured using the optical colors of RGB stars (§2.1), and C/O is estimated using the near-IR colors of TP-AGB stars.

This relationship may be less reliable in populations that have a high fraction of very dusty C stars. A large dust mass veils molecular features, causing C stars to

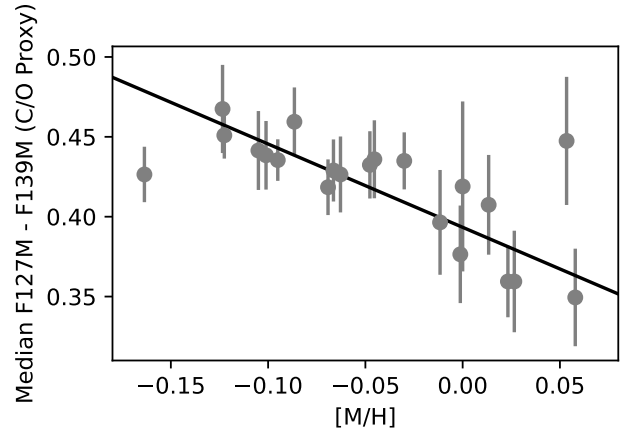


**Figure 7.** Atmospheric C/O proxy using the median F127M–F139M color of C stars for each field. The outliers at the high and low metallicity ends are Fields 1 and 20, respectively. The fitted line (Equation 3) excludes those fields. Metallicity is from Gregersen et al. (2015), see Section 2.1.

move to the upper right of the C star box marked in Figure 4. However, most galaxies studied show that stars this dusty comprise  $\lesssim 5\%$  of the C star population (Boyer et al. 2011; Srinivasan et al. 2016; Boyer et al. 2017).

##### 4.2. C/M Across M31

TP-AGB models predict that C/M decreases with increasing metallicity (Karakas et al. 2002; Marigo et al. 2013; Choi et al. 2016). This trend is caused both by a higher abundance of free oxygen in metal-rich stellar atmospheres available to bind any carbon into the CO molecule and by lower dredge up depth resulting in less carbon transported to the surface. Figure 8 shows that in M31 C/M indeed decreases smoothly with increasing metallicity in our fields. Several other studies have also observed C/M in M31, both in the northeast disk (5–18 kpc; Hamren et al. 2015) and along the southwest axis (5–40 kpc; Brewer et al. 1995; Battinelli et al. 2003; Nowotny et al. 2001). These studies also show a decrease with C/M at lower galactocentric distances, and therefore at higher metallicities, but with a shallower slope than what we see in our fields. Here, we find a slope of  $\frac{\Delta \log(C/M)}{\Delta [M/H]} \sim -6.5$ . When fit on their own, the Battinelli et al. (2003), Brewer et al. (1995), Hamren et al. (2015) data show slopes of  $-2.87$ ,  $-2.23$ , and  $-2.63$ , respectively. This slope discrepancy is discussed further in Sections 5.1 and 5.1.2.

Most TP-AGB models also predict a metallicity ceiling above which carbon stars cannot form (Karakas et al. 2002; Marigo et al. 2013; Choi et al. 2016), though the exact metallicity of this limit has yet to be observationally confirmed. While C/M is smoothly declining towards the highest metallicity fields in our survey, we see no hint of a sharp cut-off in C/M in Figure 8 despite the

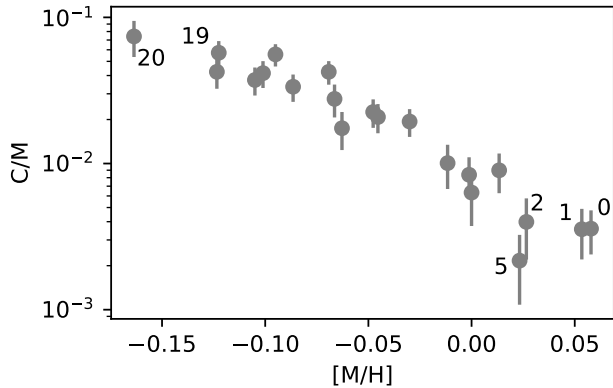


**Figure 8.**  $C/M$  vs. metallicity. The error bars on  $C/M$  reflect Poisson uncertainties. Error bars for  $[M/H]$  are not included for clarity, but are discussed in more detail in §2.1.  $C/M$  decreases smoothly as metallicity increases, with no hint at a sharp C star metallicity ceiling in these fields. The lowest and highest metallicity fields are marked with the field number.

higher metallicities reached by our fields compared to previous studies ( $\sim 4\text{--}8\times$  higher  $[M/H]$ ). Nevertheless, the  $C/M$  ratio in the innermost fields reveal an incredibly low carbon star formation efficiency, with fewer than 10 carbon stars forming among 1000–2500 M giant stars in Fields 0–5.

## 5. DISCUSSION

### 5.1. Approaching a Metallicity Ceiling?

While no abrupt metallicity ceiling is apparent in Figure 8, placing the data in the context of other nearby star-forming galaxies shows that M31 is operating in a regime that is distinct from that of its more metal-poor counterparts. In Figure 9, we show  $C/M$  vs.  $[M/H]$  for star-forming galaxies from Groenewegen (2006) and Boyer et al. (2017). The M31 data fall well below the  $C/M$  extrapolated from the more metal-poor galaxies, by more than a factor of 10 in our innermost fields. A fit to  $C/M$  vs.  $[M/H]$  reveals a slope of  $\frac{\Delta \log(C/M)}{\Delta [M/H]} \sim -1.1$  for the metal-poor galaxies, compared to a slope of  $-6.5$  for the M31 fields.

This change in slope points to a shift in the dredge-up efficiency in M31 TP-AGB stars. One result of less efficient dredge up is lower yields of the products from TP-AGB nucleosynthesis. TP-AGB stars are major contributors of light elements (C, Ne, N, Na, O, Mg, F, Al) and the main contributors of  $s$ -process elements (Rb, Ba, Sr, La, Y, Ce, Zr, Pb) (Cristallo et al. 2011; Fishlock et al. 2014). Lower yields of these elements will affect the subsequent chemical evolution of the host galaxy. Moreover, the severe lack of carbon stars will result in a lack of carbon dust formation, affecting the galactic dust budget. Having fewer C stars also has consequences for a galaxy’s integrated light, especially in the rest-frame near- and

mid-IR (e.g. Boyer et al. 2011). Given that TP-AGB stars are responsible for up to 70% of a galaxy’s integrated light (Melbourne et al. 2012; Melbourne & Boyer 2013), this shift in the color can have a major impact on the appearance of galaxies.

#### 5.1.1. Disentangling the roles of Age and Metallicity

The fraction of carbon stars is sensitive to the age of the population as well as the metallicity, making the driver of the  $C/M$  trend seen in §4.2 uncertain. Most galaxy disks are thought to form inside-out, resulting in both older ages and higher metallicities in their centers. As a result, it can be challenging to decouple these two parameters when tracking  $C/M$  across a disk. Carbon stars are predicted to form only in a narrow age range of approximately 200 Myr to 4 Gyr, whereas M-type TP-AGB stars can have ages anywhere from 55 Myr to 13 Gyr (Karakas & Lugaro 2016). These mass differences make the  $C/M$  ratio sensitive to the relative star-formation rates over these epochs. It is therefore possible that at least some of the trend in  $C/M$  in Figure 8 could be due to a variation in age rather than a variation in metallicity.

While it appears that all of our fields include ages that produce carbon stars, we can further assess the age of our fields and how it affects  $C/M$  by calculating an age proxy: the ratio of TP-AGB stars to RGB stars. This fraction is expected to be lower in populations with a higher fraction of old stars because the TP-AGB phase has a limited lifespan ( $\lesssim 3$  Myr, e.g., Kalirai et al. 2014; Cristallo et al. 2015). We define  $N_{\text{AGB}}$  as the combined number of M and C stars, and  $N_{\text{RGB}}$  as the number of stars below the TRGB with  $F814W - F110W > 0.5$  to avoid young main sequence stars and  $F110W < 22$  mag to avoid issues with crowding and incompleteness. The resulting age proxy is plotted against deprojected radius in Figure 10. As expected, the innermost fields are older than the outer fields, on average. We also see a hint of a younger population in the 5 kpc star-forming ring.

This age proxy is plotted against  $C/M$  in the right-hand panel of Figure 11. Both age and metallicity show a strong correlation with  $C/M$  in our fields, which was also shown in the outer regions of M31 by Hamren et al. (2015). The correlation matrix derived using a Spearman rank correlation coefficient shows that the degree of correlation between  $C/M$  and  $[M/H]$  is higher (96%) than between  $C/M$  and age (82%). Therefore, while age is clearly important, metallicity is the stronger effect on  $C/M$  in M31. A detailed analysis that takes M31’s star-formation history into account is being pursued in a forthcoming paper (Chen et al., in preparation).

#### 5.1.2. Ruling out Differences in $C/M$ Measurement Techniques

One could be concerned that the change in slope in Figure 9 is due to differences in classification strategies. In contrast to our near-IR HST technique, most carbon

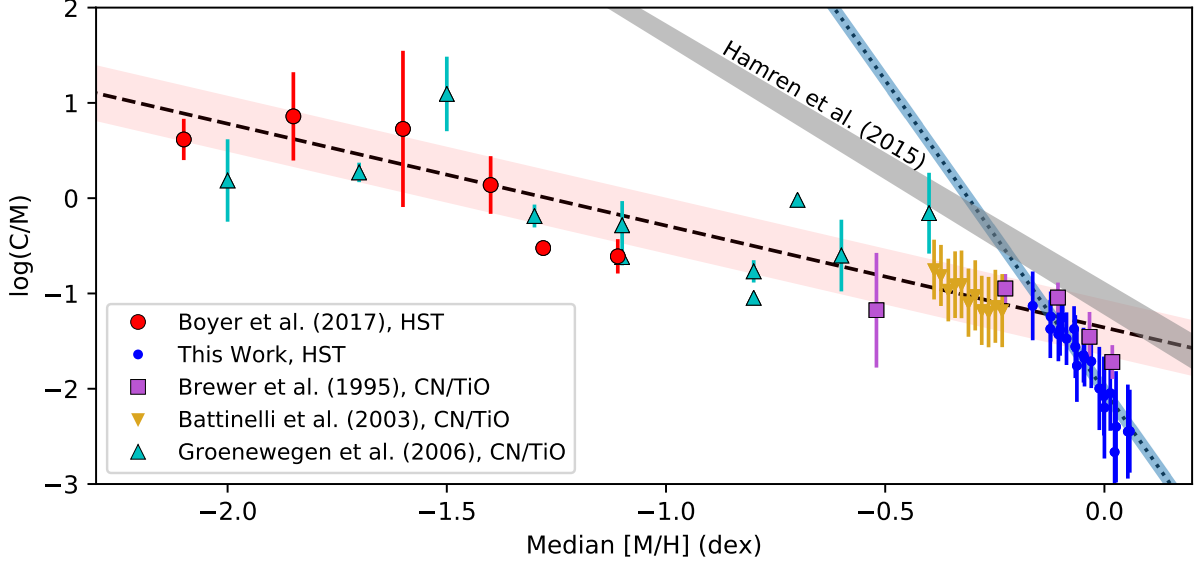


**Figure 9.**  $C/M$  ratio across the Local Group. Nearby star-forming dwarf galaxies are marked by red circles (Boyer et al. 2017) and cyan triangles (Groenewegen 2006). M31 data on the southwest side of the disk are marked by purple squares (Brewer et al. 1995) and yellow triangles (Battinelli et al. 2003), and the  $C/M$  from this work in the northeast side of the disk is marked by small blue dots. The red circles and blue dots were both measured using the HST medium-band technique to identify carbon stars, while the yellow triangles and cyan squares use optical narrow-band filters. Error bars reflect Poisson uncertainties. The dashed line and red shaded region mark the best fit and  $1\text{-}\sigma$  error for the dwarf galaxies, and the dotted line and blue shaded region mark the same for our fields in M31 (blue points only). The gray shaded region marks the  $C/M$  vs. metallicity slope measured in the outer disk of M31 by Hamren et al. (2015) using spectroscopy to identify carbon stars. It is clear that M31 does not follow the trend set by the more metal-poor galaxies, indicating that the carbon star formation efficiency drops substantially at high metallicity.

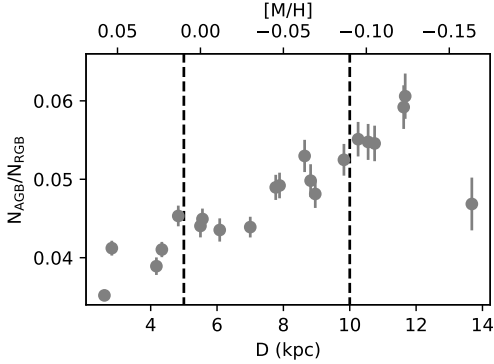


**Figure 10.**  $N_{AGB}/N_{RGB}$  as a population age proxy, plotted against deprojected distance. Lower values of  $N_{AGB}/N_{RGB}$  indicate an older population. The 5 and 10 kpc star-forming rings are marked with dashed lines. As expected, the inner fields are generally older than the outer fields.

star surveys in the Local Group use optical narrow-band filters centered on CN and TiO bands to identify carbon stars, including data from Brewer et al. (1995), Battinelli et al. (2003) and Groenewegen (2006). We must

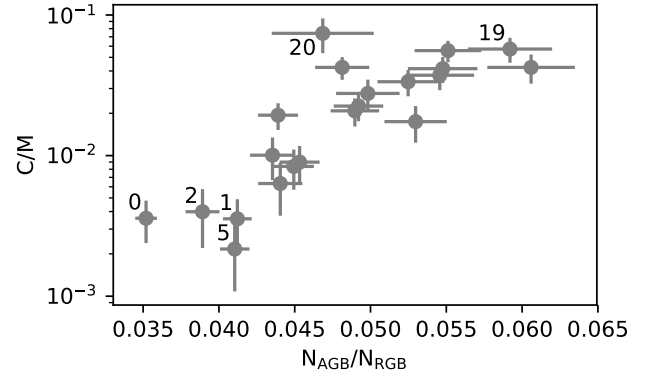


**Figure 11.**  $C/M$  vs. an age proxy ( $N_{AGB}/N_{RGB}$ ), with error bars reflecting Poisson uncertainties. Both the age and metallicity are correlated with  $C/M$ , though metallicity shows the stronger correlation. In both panels, the lowest and highest metallicity fields are marked with the field number.

therefore verify that our HST medium-band data can be directly compared to the optical CN/TiO data.

The major difference among these strategies is the identification of M giant stars, as noted in Section 3.4.1. Another notable distinction lies in the fact that the opti-

cal data are not sensitive to stars with a high amount of optical extinction from circumstellar dust, which pushes both M-giants and C stars below the TRGB. However, stars dusty enough to veil molecular features are rare (typically  $<5\%$ ; Boyer et al. 2011; Srinivasan et al. 2016; Boyer et al. 2017), so the effect on C/M is expected to be small.

Despite these differences, C/M measured using both near-IR and optical techniques agree very well in metal-poor galaxies (red circles and cyan triangles in Fig. 9). This agreement is due to a lack of late-type M giants in metal-poor galaxies and to weaker TiO absorption in metal-poor stars at a given  $T_{\text{eff}}$ , minimizing the effect of the M star definition on C/M. Metal-poor M giants fall along a warmer Hayashi line (Marigo et al. 2013), rarely reaching spectral types later than approximately M3, though a few exceptions exist in the Magellanic Clouds (Marshall et al. 2004; van Loon et al. 2005; Goldman et al. 2017). Since only late-type M giants fall below the TRGB in Figure 6, the C/M ratio remains largely unaffected by details of choices of M star selections at low metallicity.

In contrast, the disagreement in C/M grows at the high metallicity end, resulting in the different values measured by different surveys in M31 (note especially the offsets between this work, Brewer et al. (1995), and Hamren et al. (2015) in Fig. 9 at  $[M/H] > -0.25$ ). Nevertheless, both techniques indicate a shift to a steeper C/M slope in M31 compared to metal-poor galaxies, an effect that was not noted in the previous M31 studies despite, e.g., the Brewer et al. (1995) data showing a shift in slope in their 2 innermost fields. We therefore do not believe that the change in slope in M31 is due to sample selection.

### 5.2. Constraining Carbon Star Formation Efficiency

As already noted, TP-AGB models predict a maximum metallicity limit for carbon star formation. The exact limit is dictated by uncalibrated model details, and is caused by a higher oxygen abundance, less-efficient dredge up, and a late onset of the third dredge-up. These characteristics prevent atmospheric C/O from exceeding unity before mass loss terminates the TP-AGB phase (Karakas et al. 2002; Marigo et al. 2013). Our results show that the metallicity ceiling is a gradual shift, rather than an abrupt limit. An inflection point in carbon star formation efficiency, as indicated by the change in C/M slope in Figure 9, falls between the metallicities of the LMC and M31’s disk, suggesting that M33

could be an interesting environment in which to probe this transition, given its intermediate metallicity. The Brewer et al. (1995) and Battinelli et al. (2003) data, and perhaps even Field 20, already show a hint that this transition occurs in the outermost region of M31’s disk, possibly between the 10 kpc and 15 kpc rings (Fig. 1).

On the high metallicity end, a hard limit for carbon star formation remains elusive. Observations nearer to M31’s bulge are likely the best chance at identifying a limit since more distant galaxies suffer from severe crowding and since the motion of large convective cells on the stellar surface result in uncertain Gaia distance estimates to TP-AGB stars in the Milky Way (Chiavassa et al. 2011, 2018).

## 6. CONCLUSIONS

We have surveyed 20 fields in the disk of M31 ( $R = 2.6\text{--}13.7$  kpc) with HST’s WFC3/IR camera to identify and classify TP-AGB stars. We use the medium-band filters described in more detail in Boyer et al. (2013, 2017) to separate carbon-rich (C) from oxygen-rich (M) TP-AGB stars and find that the ratio of the two (C/M) decreases rapidly with galactic radius, resulting in a C/M that is more than a factor of 10 lower than predicted by observations in more metal-poor galaxies. The shift to a more rapid decline in C/M with  $[M/H]$  appears to occur just beyond the 10 kpc star-forming ring, corresponding to  $[M/H] > -0.1$  dex when assuming the metallicity gradient derived by Gregersen et al. (2015). Despite this rapid decline in C/M, carbon stars are still (inefficiently) forming in M31 even at 2.6 kpc ( $[M/H] \sim +0.06$ ). These observations provide a robust constraint to models of TP-AGB stars, though the predicted metallicity ceiling for carbon star formation remains elusive.

Support for HST program GO-14072 was provided by NASA through a grant from the Space Telescope Science Institute, which is operated by the Association of Universities for Research in Astronomy, Incorporated, under NASA contract NAS5-26555. PM, LG, BA, and YC acknowledge the support from the ERC Consolidator Grant scheme (project STARKEY, G. A. n 615604). PR acknowledges support from the National Science Foundation under Award No. 1501205. DRW is supported by a fellowship from the Alfred P. Sloan Foundation and acknowledges support from the Alexander von Humboldt Foundation.

## REFERENCES

- Aringer, B., Girardi, L., Nowotny, W., Marigo, P., & Bressan, A. 2016, *MNRAS*, 457, 3611
- Aringer, B., Girardi, L., Nowotny, W., Marigo, P., & Lederer, M. T. 2009, *A&A*, 503, 913
- Baldwin, C., McDermid, R. M., Kuntschner, H., Maraston, C., & Conroy, C. 2017, *Monthly Notices of the Royal Astronomical Society*, 473, 4698

- Barmby, P., Ashby, M. L. N., Bianchi, L., et al. 2006, *ApJL*, 650, L45
- Battinelli, P., & Demers, S. 2005, *A&A*, 434, 657
- Battinelli, P., Demers, S., & Letarte, B. 2003, *AJ*, 125, 1298
- Blum, R. D., Mould, J. R., Olsen, K. A., et al. 2006, *AJ*, 132, 2034
- Boothroyd, A. I., & Sackmann, I.-J. 1988, *ApJ*, 328, 632
- Boyer, M. L., Srinivasan, S., van Loon, J. Th., et al. 2011, *AJ*, 142, 103
- Boyer, M. L., Srinivasan, S., Riebel, D., et al. 2012, *ApJ*, 748, 40
- Boyer, M. L., Girardi, L., Marigo, P., et al. 2013, *ApJ*, 774, 83
- Boyer, M. L., McQuinn, K. B. W., Groenewegen, M. A. T., et al. 2017, *ApJ*, 851, 152
- Bressan, A., Marigo, P., Girardi, L., et al. 2012, *MNRAS*, 427, 127
- Bressan, A., Tang, J., Slemmer, A., et al. 2014, *Monthly Notices of the Royal Astronomical Society*, 445, 4287
- Brewer, J. P., Richer, H. B., & Crabtree, D. R. 1995, *AJ*, 109, 2480
- Cardelli, J. A., Clayton, G. C., & Mathis, J. S. 1989, *ApJ*, 345, 245
- Chen, Y., Girardi, L., Bressan, A., et al. 2014, *MNRAS*, 444, 2525
- Chiavassa, A., Freytag, B., & Schultheis, M. 2018, *A&A*, 617, L1
- Chiavassa, A., Pasquato, E., Jorissen, A., et al. 2011, *A&A*, 528, A120
- Choi, J., Dotter, A., Conroy, C., et al. 2016, *ApJ*, 823, 102
- Cioni, M.-R. L. 2009, *A&A*, 506, 1137
- Conroy, C., Gunn, J. E., & White, M. 2009, *ApJ*, 699, 486
- Cristallo, S., Straniero, O., Piersanti, L., & Gobrecht, D. 2015, *ApJS*, 219, 40
- Cristallo, S., Piersanti, L., Straniero, O., et al. 2011, *ApJS*, 197, 17
- Dalcanton, J. J., Williams, B. F., Melbourne, J. L., et al. 2012a, *ApJS*, 198, 6
- Dalcanton, J. J., Williams, B. F., Lang, D., et al. 2012b, *ApJS*, 200, 18
- Dolphin, A. E. 2000, *PASP*, 112, 1383
- Dorman, C. E., Guhathakurta, P., Fardal, M. A., et al. 2012, *ApJ*, 752, 147
- Fishlock, C. K., Karakas, A. I., Lugaro, M., & Yong, D. 2014, *ApJ*, 797, 44
- Fluks, M. A., Plez, B., The, P. S., et al. 1994, *A&AS*, 105, 311
- Girardi, L., Dalcanton, J., Williams, B., et al. 2008, *PASP*, 120, 583
- Goldman, S. R., van Loon, J. Th., Zijlstra, A. A., et al. 2017, *MNRAS*, 465, 403
- Gregersen, D., Seth, A. C., Williams, B. F., et al. 2015, *AJ*, 150, 189
- Groenewegen, M. A. T. 2006, *A&A*, 448, 181
- Hamren, K. M., Rockosi, C. M., Guhathakurta, P., et al. 2015, *ApJ*, 810, 60
- Johnson, B. D., Weisz, D. R., Dalcanton, J. J., et al. 2013, *ApJ*, 772, 8
- Kalirai, J. S., Marigo, P., & Tremblay, P.-E. 2014, *ApJ*, 782, 17
- Karakas, A. I. 2014, *MNRAS*, 445, 347
- Karakas, A. I., & Lattanzio, J. C. 2014, *PASA*, 31, e030
- Karakas, A. I., Lattanzio, J. C., & Pols, O. R. 2002, *PASA*, 19, 515
- Karakas, A. I., & Lugaro, M. 2016, *ApJ*, 825, 26
- Karakas, A. I., Lugaro, M., Carlos, M., et al. 2018, *MNRAS*, 477, 421
- Lewis, A. R., Dolphin, A. E., Dalcanton, J. J., et al. 2015, *ApJ*, 805, 183
- Marigo, P., Bressan, A., Nanni, A., Girardi, L., & Pumo, M. L. 2013, *MNRAS*, 434, 488
- Marshall, J. R., van Loon, J. Th., Matsuura, M., et al. 2004, *MNRAS*, 355, 1348
- Matsuura, M., Barlow, M. J., Zijlstra, A. A., et al. 2009, *MNRAS*, 396, 918
- McConnachie, A. W., Irwin, M. J., Ferguson, A. M. N., et al. 2005, *MNRAS*, 356, 979
- McQuinn, K. B. W., Boyer, M. L., Skillman, E. D., & Dolphin, A. 2019, *ApJ*, submitted
- McQuinn, K. B. W., Boyer, M. L., Mitchell, M. B., et al. 2017, *ApJ*, 834, 78
- Melbourne, J., & Boyer, M. L. 2013, *ApJ*, 764, 30
- Melbourne, J., Williams, B. F., Dalcanton, J. J., et al. 2012, *ApJ*, 748, 47
- Méndez, B., Davis, M., Moustakas, J., et al. 2002, *AJ*, 124, 213
- Nanni, A., Bressan, A., Marigo, P., & Girardi, L. 2013, *MNRAS*, 434, 2390
- Nanni, A., Marigo, P., Groenewegen, M. A. T., et al. 2016, *MNRAS*, 462, 1215
- Nataf, D. M., Udalski, A., Gould, A., & Pinsonneault, M. H. 2011, *ApJ*, 730, 118
- Nowotny, W., Kerschbaum, F., Schwarz, H. E., & Olofsson, H. 2001, *A&A*, 367, 557
- Pastorelli, G., Marigo, P., Girardi, L., et al. 2019, *MNRAS*, submitted

- Pietrinferni, A., Cassisi, S., Salaris, M., Cordier, D., & Castelli, F. 2007, in IAU Symposium, Vol. 241, *Stellar Populations as Building Blocks of Galaxies*, ed. A. Vazdekis & R. Peletier, 39–40
- Rosenfield, P., Marigo, P., Girardi, L., et al. 2016, *ApJ*, 822, 73
- Rosenfield, P., Johnson, L. C., Girardi, L., et al. 2012, *ApJ*, 755, 131
- Rosenfield, P., Marigo, P., Girardi, L., et al. 2014, *ApJ*, 790, 22
- Saglia, R. P., Opitsch, M., Fabricius, M. H., et al. 2018, *A&A*, 618, A156
- Sanders, N. E., Caldwell, N., McDowell, J., & Harding, P. 2012, *ApJ*, 758, 133
- Schlegel, D. J., Finkbeiner, D. P., & Davis, M. 1998, *ApJ*, 500, 525
- Schneider, R., Valiante, R., Ventura, P., et al. 2014, *MNRAS*, 442, 1440
- Sirianni, M., Jee, M. J., Benítez, N., et al. 2005, *PASP*, 117, 1049
- Srinivasan, S., Boyer, M. L., Kemper, F., et al. 2016, *MNRAS*, 457, 2814
- van Loon, J. Th., Cioni, M.-R. L., Zijlstra, A. A., & Loup, C. 2005, *A&A*, 438, 273
- Ventura, P., & Marigo, P. 2010, *MNRAS*, 408, 2476
- Weiss, A., & Ferguson, J. W. 2009, *A&A*, 508, 1343
- Williams, B. F., Lang, D., Dalcanton, J. J., et al. 2014, *ApJS*, 215, 9
- Williams, B. F., Dolphin, A. E., Dalcanton, J. J., et al. 2017, *ApJ*, 846, 145
- Zhukovska, S., & Henning, T. 2013, *A&A*, 555, A99
- Zurita, A., & Bresolin, F. 2012, *MNRAS*, 427, 1463

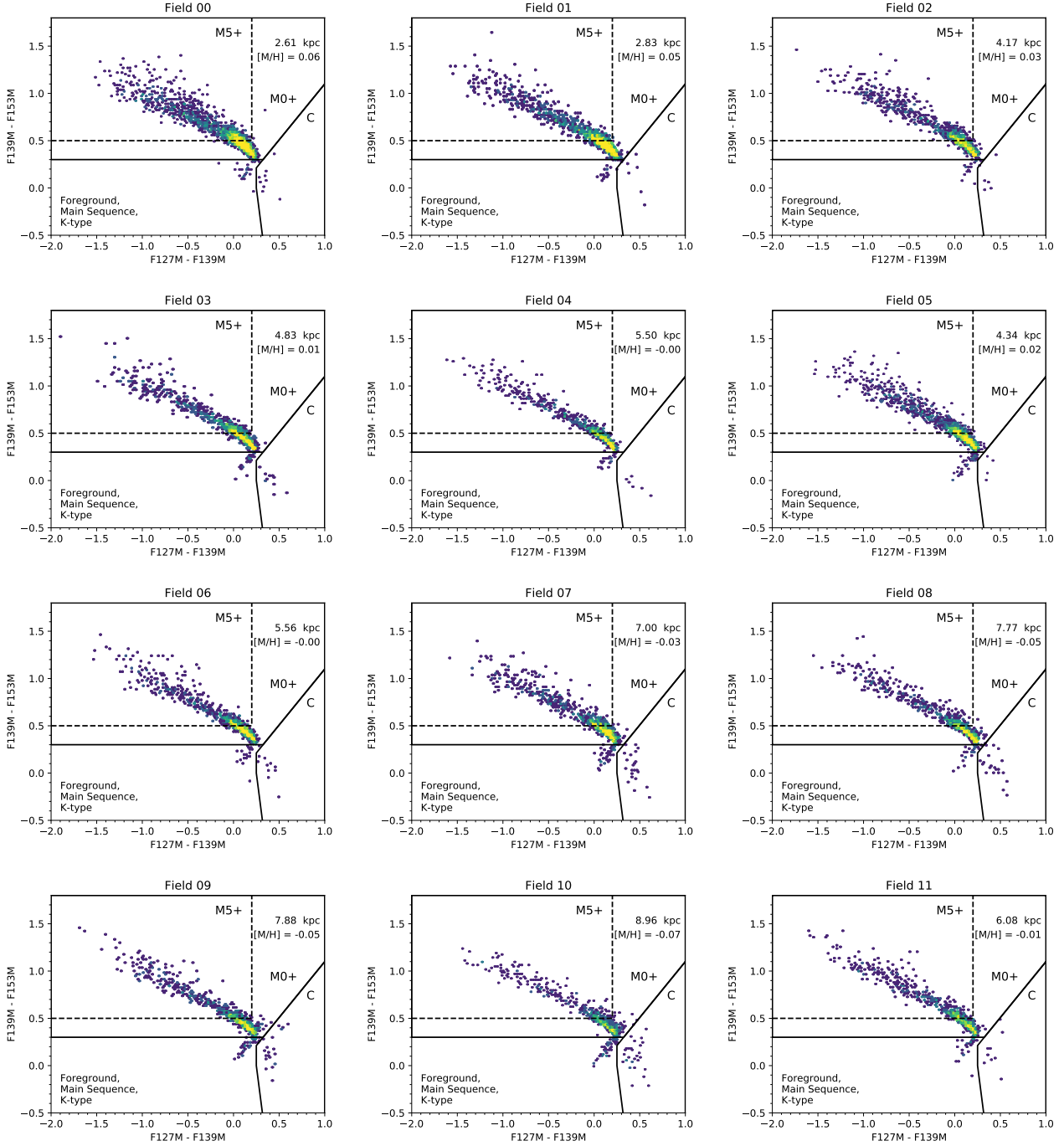


**Figure 12.** Medium-band IR CCDs for Fields 0–11. As in Figure 4, only stars brighter than one of the near-IR TRGBs are included. Solid lines separate M-type from C-type TP-AGB stars and other contaminating sources (Foreground, main sequence, and K-type). Stars to the left of the dashed line are late-type M giants (later than M5).

## APPENDIX

### A. IR MEDIUM-BAND COLOR-COLOR DIAGRAMS

We include here the color-color diagrams (CCDs) constructed from all 21 fields, including the pilot field (Field 0). Figure 4 combines all fields into a single CCD.

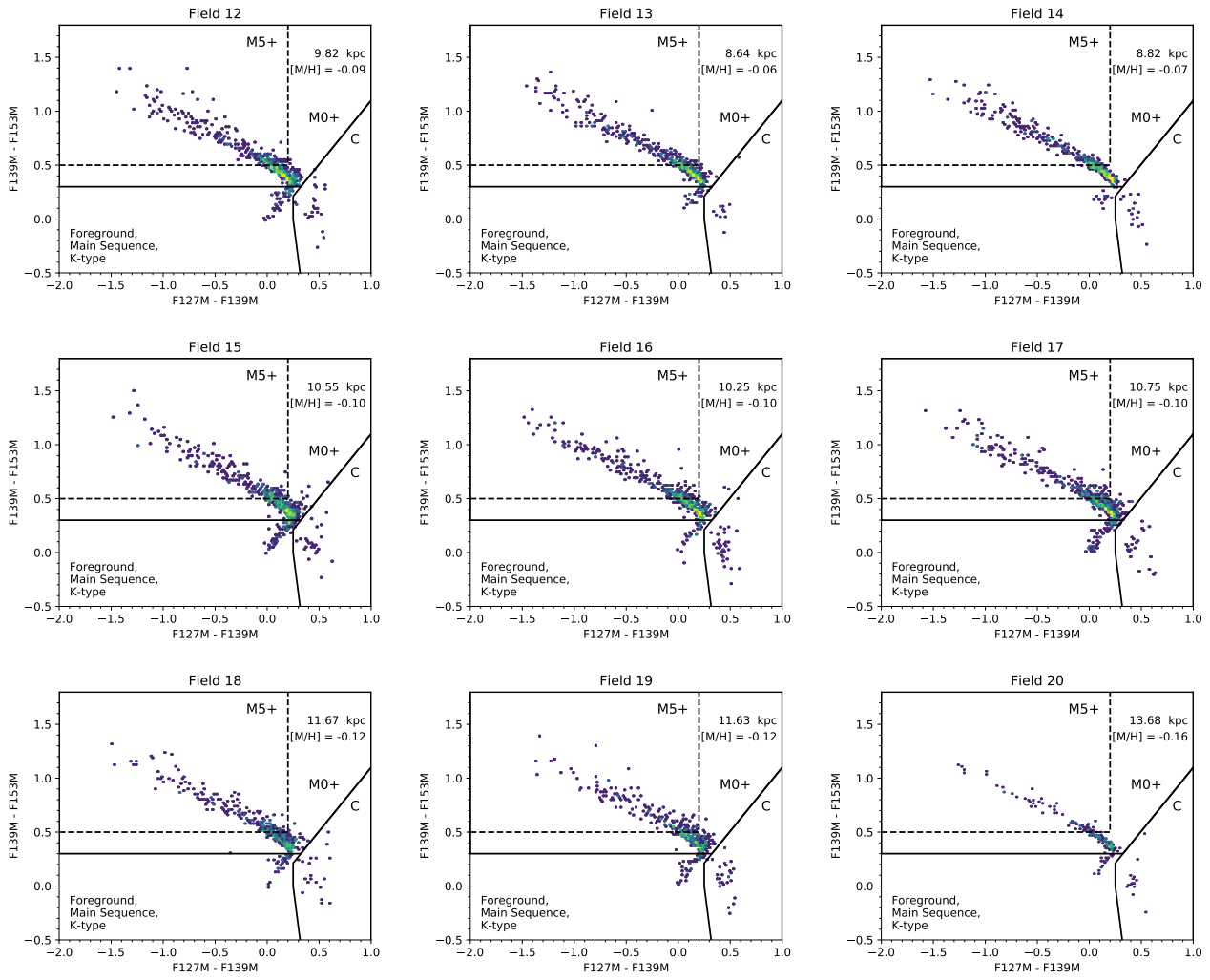


Figure 13. Same as Figure 12, for Fields 12-20.